

Modeling hydrodynamics, magnetic fields and synthetic radiographs for high-energy-density plasma flows in shock-shear targets

Yingchao Lu,^{1,2,*} Shengtai Li,^{1,†} Hui Li,^{1,‡} Kirk A. Flippo,^{3,§} Dan Barnak,³

Andrew Birkel,⁴ Brandon Lahmann,⁴ Chikang Li,⁴ Alexander M. Rasmus,⁵

Kwyntero Kelso,⁵ Alex Zylstra,⁶ Edison Liang,² Petros Tzeferacos,⁷ and Don Lamb⁷

¹*Theoretical Division, Los Alamos National Laboratory, Los Alamos, New Mexico 87545, USA*

²*Department of Physics and Astronomy, Rice University, Houston, Texas 77005, USA*

³*Laboratory for Laser Energetics, Rochester, New York 14623, USA*

⁴*Plasma Science and Fusion Center, Massachusetts Institute of Technology, Cambridge, Massachusetts 02139, USA*

⁵*Physics Division, Los Alamos National Laboratory, Los Alamos, New Mexico 87545, USA*

⁶*Lawrence Livermore National Laboratory, Livermore, California 94550, USA*

⁷*Department of Astronomy and Astrophysics, University of Chicago, Chicago, Illinois 60637, USA*

(Dated: November 22, 2019)

Three-dimensional FLASH radiation-magnetohydrodynamics (radiation-MHD) modeling is carried out to study the hydrodynamics and magnetic fields in the shock-shear derived platform. Simulations indicate that fields of tens of Tesla can be generated via Biermann battery effect due to vortices and mix in the counter-propagating shock-induced shear layer. Synthetic proton radiography simulations using MPRAD and synthetic X-ray image simulations using SPECT3D are carried out to predict the observable features in the diagnostics. Quantifying the effects of magnetic fields in inertial confinement fusion (ICF) and high-energy-density (HED) plasmas represents frontier research that has far-reaching implications in basic and applied sciences.

I. INTRODUCTION

When an inertial confinement fusion (ICF) capsule implodes, the material turns into dense plasmas and recent simulations have shown that such plasmas tend to be unstable and turbulence can develop[1]. Even though it is debated whether turbulence is damped by the viscosity in the hot spot, the shocked interfaces as well as the interface between the shell and the hot spot can have very different dynamics and can indeed be unstable[2–7]. It is believed that turbulence and the associated mixing process can be crucial for understanding ICF.

The Biermann battery effect[8] is known to generate seed magnetic fields in laser driven plasma flows and has been studied extensively in high-energy-density (HED) laser-driven experiments[9–16], but the strength and importance of these fields in the close to or higher than solid density plasmas such as an ICF implosion are not well known. Three-dimensional extended-magnetohydrodynamic (extended-MHD) simulations of the stagnation phase of ICF including Biermann battery term[8], Nernst term[17] and anisotropic heat conduction in the magnetic field, indicate that self-generated magnetic fields can reach over 10^4 Tesla and can affect the electron heat flow[18]. The simulations with pre-magnetization for ICF implosions show the significance of Lorentz force and α -particle trapping[19]. In low density laser driven plasmas, the magnetic field can be am-

plified by turbulence and measured using temporal diagnostics by B-dot probe[20] and spatial diagnostics by proton radiography[21]. The magnetic frequency spectrum in supersonic plasma turbulence has been measured in a recent experiment[22] on the Vulcan laser. However, in those experiments[20–22] the magnetic field is not high enough to change the dynamics of the hydrodynamical flow.

In this work, we use the shock-shear platform[23, 24] developed at Los Alamos National Laboratory (LANL) to quantify the dynamics of magnetic fields in HED plasmas with instabilities and turbulence. The shock compression can achieve a regime where the density is around 1g/cc . The targets with large density can diffuse the proton beam and affect the interpretation of the proton image[25], but the simulations for the synthetic proton image including the stopping power and Coulomb scattering show that the deflection of proton beam by magnetic fields is still detectable. Further improvements are still needed to make the fields high enough to change the dynamics of the small-scale evolution of vortices like those in a turbulent cascade, and affect our understanding of turbulence.

The shock-shear platform[23, 24], as a platform to isolatedly study the shear-induced instabilities and turbulence production under HED conditions, i.e. pressure larger than 1Mbar , has been used to investigate the turbulent mixing[26, 27] at material interfaces when subject to multiple shocks and reshocks or high-speed shear[23, 28]. The experiments[29–33] using the shock-shear platform has been carried out on the OMEGA Laser Facility and National Ignition Facility (NIF). These experiments provide quantitative measurements to assist in validation efforts[34–36] for mix models, such as Besnard-Harlow-Rauenzahn (BHR) model[37, 38]. The

* yclu@lanl.gov

† sli@lanl.gov

‡ hli@lanl.gov

§ kflippo@lanl.gov

experimental data and the validation efforts constrain models relevant to integrated HED experiments such as ICF or astrophysical problems. In the shock-shear targets, the Biermann Battery ($\nabla n_e \times \nabla T_e$) term[8] can generate and sustain strong magnetic fields in the vortices due to the misalignment of the density gradient and temperature gradient caused by electron heat conduction. However, the magnetic fields in the shock-shear targets have not been quantified in simulations or experiments.

In this work, we use the radiation-MHD code FLASH[39, 40] to model the evolution of the shock-shear system on OMEGA[41]. The experiment simulated in this paper uses 8 beams each with 500J energy laser ablation in 1ns on each side to drive strong adjacent contour-propagating shocks. Kelvin-Helmholtz instability laterally spreads across a thin layer of magnesium, copper or plastic placed at the interface. The layer is cut with slots to seed the initial density perturbation, which can generate vortices during the evolution of the shock and shear. The temperature of the materials reaches tens of electron-volts, and simulations predict the Mach number of the post-shock flows in the experiment is around 2 on each side of the shear layer. The magnetic field is generated by the Biermann battery term[8] and dissipated by the resistive term. The X-ray image[42–44] and the proton radiography[9] are predicted and will be compared to the experimental data in a later paper.

This paper is organized as follows. Sec II describes simulation methods and the configuration of the target system. In Sec III, we show the results for hydrodynamics and MHD evolution from FLASH, the synthetic X-ray image using SPECT3D and the synthetic proton radiography using MPRAD. The conclusions and discussions is given in Sec IV.

II. SIMULATION METHODS AND CONFIGURATION

The FLASH code[39, 40][45] is used to carry out the detailed physics simulations of our laser experiments to study the dynamics of the shock-shear system. FLASH is a publicly available, multi-physics, highly scalable parallel, finite-volume Eulerian code and framework whose capabilities include: adaptive mesh refinement (AMR), multiple hydrodynamic and MHD solvers[46–49], implicit solvers for diffusion using the HYPRE library[50] and laser energy deposition. FLASH is capable of using multi-temperature equation of states and multi-group opacities. To simulate laser-driven High-Energy-Density-Physics (HEDP) experiments, a 3T treatment, i.e. $T_{\text{rad}} \neq T_{\text{ele}} \neq T_{\text{ion}}$, is usually adopted. The equations which FLASH solves to describe the evolution of the 3T magnetized plasma are

$$\frac{\partial \rho}{\partial t} + \nabla \cdot (\rho \mathbf{v}) = 0 \quad (1)$$

$$\frac{\partial \rho \mathbf{v}}{\partial t} + \nabla \cdot (\rho \mathbf{v} \mathbf{v} - \frac{1}{4\pi} \mathbf{B} \mathbf{B}) + \nabla P_{\text{tot}} = 0 \quad (2)$$

$$\begin{aligned} & \frac{\partial \rho E_{\text{tot}}}{\partial t} + \nabla \cdot (\mathbf{v}(\rho E_{\text{tot}} + P_{\text{tot}}) - \frac{1}{4\pi} \mathbf{B}(\mathbf{v} \cdot \mathbf{B})) \\ & - \frac{1}{4\pi} \nabla \cdot (\mathbf{B} \times (\eta \nabla \times \mathbf{B})) - \frac{1}{4\pi} \nabla \cdot (\mathbf{B} \times \frac{c}{e} \frac{\nabla P_e}{n_e}) = -\nabla \cdot \mathbf{q} + S \end{aligned} \quad (3)$$

$$\begin{aligned} & \frac{\partial \mathbf{B}}{\partial t} + \nabla \cdot (\mathbf{v} \mathbf{B} - \mathbf{B} \mathbf{v}) = \\ & -\nabla \times (\eta_B \nabla \times \mathbf{B}) + \frac{c}{e} \nabla \times \frac{\nabla P_e}{n_e} \end{aligned} \quad (4)$$

where the total pressure is given by $P_{\text{tot}} = P_{\text{ion}} + P_{\text{ele}} + P_{\text{rad}} + \frac{1}{8\pi} B^2$, and the total specific energy $E_{\text{tot}} = e_{\text{ion}} + e_{\text{ele}} + e_{\text{rad}} + \frac{1}{8\pi} B^2 + \frac{1}{2} \mathbf{v} \cdot \mathbf{v}$. The total heat flux \mathbf{q} is the summation of electron heat flux $\mathbf{q}_e = -\kappa \nabla T_{\text{ele}}$ and radiation flux \mathbf{q}_r , where κ is the Spitzer electron heat conductivity[51, 52]. The flux-limit used for electron thermal conduction is set to be 6% of the free streaming flux $q_{FS} = n_e k_B T_e \sqrt{\frac{k_B T_e}{m_e}}$. The first term on the R.H.S of Eq(4) contains the Spitzer magnetic resistivity η_B [51, 52]. The second term on the R.H.S of Eq(4) is the Biermann Battery term, which generates the magnetic field even if there is no seed magnetic field initially. The plasma has zero initial magnetic field in the simulations. Because plasma beta β is much larger than unity, the Hall term is neglectable and not included in the simulations. The Biermann battery term is turned off in the cells adjacent to the shock detected numerically[53]. The magnetic fields generation near the shock is not calculated because of the convergence problem[54] for calculating Biermann battery term on the Eulerian grid. The convergence problem might be resolved on a Lagrangian grid. On the other hand, the shock in this work is highly collisional and with small thickness compared to the spatial resolution of proton radiography, thus the scale of the magnetic field near the shock is too small to be detectable. The energy equations for the three components are

$$\frac{\partial}{\partial t} (\rho e_{\text{ion}}) + \nabla \cdot (\rho e_{\text{ion}} \mathbf{v}) + P_{\text{ion}} \nabla \cdot \mathbf{v} = \rho \frac{c_{v,\text{ele}}}{\tau_{ei}} (T_{\text{ele}} - T_{\text{ion}}) \quad (5)$$

$$\begin{aligned} & \frac{\partial}{\partial t} (\rho e_{\text{ele}}) + \nabla \cdot (\rho e_{\text{ele}} \mathbf{v}) + P_{\text{ele}} \nabla \cdot \mathbf{v} = \rho \frac{c_{v,\text{ele}}}{\tau_{ei}} (T_{\text{ion}} - T_{\text{ele}}) \\ & -\nabla \cdot \mathbf{q}_{\text{ele}} + Q_{\text{abs}} - Q_{\text{emis}} + Q_{\text{las}} + Q_{\text{ohm}} \end{aligned} \quad (6)$$

$$\frac{\partial}{\partial t} (\rho e_{\text{rad}}) + \nabla \cdot (\rho e_{\text{rad}} \mathbf{v}) + P_{\text{rad}} \nabla \cdot \mathbf{v} = \nabla \cdot \mathbf{q}_{\text{rad}} - Q_{\text{abs}} + Q_{\text{emis}} \quad (7)$$

where $c_{v,\text{ele}}$ is the electron specific heat, τ_{ei} the ion-electron Coulomb collision time. The Q_{abs} (absorption) and Q_{emis} (emission) describes the energy transfer between the electron and the radiation, which is modeled using the multi-group flux-limited radiation diffusion. The laser absorption term Q_{las} is computed using ray-tracing in the geometric optics approximation via the

inverse-Bremsstrahlung process. Q_{ohm} is the rate of electron energy increase due to Ohmic heating. The auxiliary equations Eq(5)-(7) are advanced in time such that the distribution of energy change due to the work and the total shock-heating is based on the pressure ratio of the components, which is a method implemented in FLASH inspired by the radiation-hydrodynamics code RAGE[55, 56]. We use the equation of state and opacity table from PROPACEOS[57][58] for modeling all the material properties in our target system.

We initialize the FLASH simulation using the geometry and parameters of targets used for OMEGA experiments. The target system is composed of the shock tube, the gold cone for minimizing stray laser light, the foam filling the shock tube and a plastic cap covering the end of the tube, as shown in Fig. 1. As shown in Fig. 1c, a window is opened in the middle of the tube and along the path of the proton beam to make the proton beam less diffusive, i.e. less energy lost and scattering. However, the opened window can make the plasma squirt outwardly. We use the foam with density 62mg/cc, and the foam is divided by a layer with slanted or non-slanted slots, as shown in Fig. 1e and 1f. The end cap is 1g/cc plastic. The shape of the slots, the material and the thickness of the layer, and the material of the wall are listed in Table I. Some targets are built with a pepperpot screen (PPS)[59], as shown in Fig. 1b. The PPS is used for a narrow view of the proton deflection signal in proton radiography, reducing the signal contamination from off-center line-of-sight. The 200 μm diameter hole in the middle allows proton beams to go through the central part of the target. Other holes are used as references to register the position of protons. The PPS is a 40 μm thick tantalum foil.

In the initialization, the pressure of all the solid regions is $5 \times 10^3 \text{bar} (= 5 \times 10^9 \text{erg/cm}^3)$, and the temperature is calculated self-consistently from the equation of state table. Using the same pressure instead of the same temperature among all the solid regions can prevent one solid region from expanding into another solid region and launching artificial shocks before the high-energy-density conditions is reached. Under HED condition, the pressure is larger than $10^5 \text{bar} (= 10^{11} \text{erg/cm}^3)$, thus the initial pressure is low enough to have neglectable effect on the simulations. The vacuum region is initially filled with 10^{-6}g/cc helium to avoid numerical problems in hydrodynamics or MHD solvers. The density is low enough that the effect of helium on the simulations is negligible.

A 3D cartesian grid with $(240 \times 240 \times 464)$ zones is used to resolve a $(1440 \mu\text{m} \times 1440 \mu\text{m} \times 2784 \mu\text{m})$ domain, corresponding to 6 μm per cell width. Using AMR, each zone is adaptively refined to one leaf level, i.e. a resolution of 3 μm or $2^3 = 8$ zones, if the mass fraction of the layer material is larger than 10%. The refinement allows us to efficiently resolve the dynamics near the layer and reduce the computing time spent on the zones far away from the layer. Although we cannot resolve the turbulence dissipation scale with the current computing capability

and neither do we use Reynolds-averaging Navier-Stokes (RANS) models such as BHR model to resolve the small scale dissipation process of the fluid, FLASH is still a suitable tool for designing these experiments because the fabricated layers have low surface roughness.

To model the laser driven energy deposition, we use the spatial and temporal specifications of each of the 16 OMEGA driver beams. Ray tracing by solving the geometric optics and the inverse bremsstrahlung absorption is used. The 16 driver beams are turned on and turned off simultaneously with a 1ns pulse duration and 8 beams on each side of the target. Each delivers 500J of energy on a target. The radius of each beam is 283 μm and the intensity distribution we use is gaussian.

For convention, $t = 0$ is the time for laser turn on. The axis of the shock tube is the z axis. The layer dividing the foam is in the $y - z$ plane, i.e. the plane with $x = 0$ everywhere. The center of the target is at $x = y = z = 0$. The x axis extends through the window.

The primary diagnostic for temporally and spatially resolved profile of the density and shock propagation in the experiments is the point projection X-ray radiography with a vanadium backlighter at $23\times$ magnification. The backlighter source emits 5180eV and 5205eV helium like lines[60]. The images are recorded on the X-ray framing camera (XRFC)[42–44]. We use SPECT3D[61][62] to generate the synthetic ray-tracing X-ray image. The line of sight of XRFC is along the y axis, which captures the distortion of the layer.

Proton radiography[9], using D^3He (14.7 MeV) protons from fusion, measures magnetic fields. The temporal resolution of proton radiograph is typically $\sim 150\text{ps}$ and the spatial resolution is typically $\sim 45\mu\text{m}$. The diffusion of the proton beam caused by Coulomb scattering[63, 64] and stopping power[65–69] is significant for the targets we use. We use Monte Carlo code MPRAD[25] to model the synthetic proton radiography, including the Lorentz force and the effects from Coulomb scattering and stopping power. The proton source stands at $(-0.75\text{cm}, 0, 0)$, while the image plate CR39 is located 27cm from the center on the other side. The line of sight of the proton radiography is perpendicular to the line of sight of the X-ray image. The energy distribution of the proton source we use in the simulation is a gaussian distribution with $\text{FWHM} = 0.25\text{MeV}$ centered at 14.7MeV.

III. SIMULATION RESULTS

We show the results from FLASH simulations and the synthetic radiography to study the evolution and dynamics of the flows in the shock-shear targets in Fig. 2 to 4. In the synthetic radiographs, the spatial scales of the synthetic radiographs are divided by the magnification to align with the scales on the target system. The target we use in this work are different from previous shock-shear experiments[28, 30, 34, 35] mainly in two aspects: (1) cut slots in the layer for seeding density perturbation,

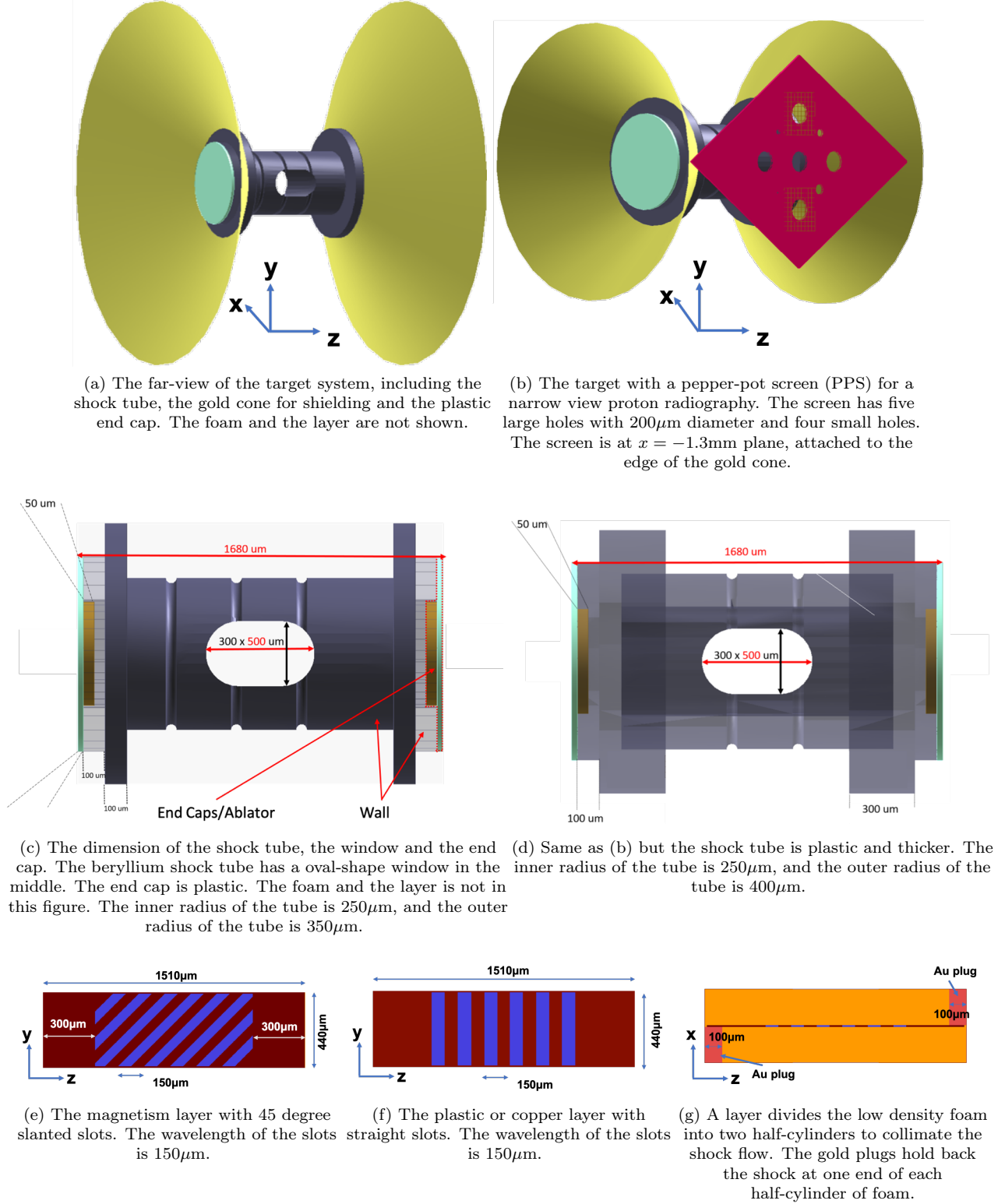


Figure 1: The experiment setup. The shapes and dimensions of different parts of the target is used to initialize the FLASH simulations.

Table I: The parameters and the maximum values of magnetic field and electron temperature for the three different targets/runs we use. T_e and B are calculated by averaging over a $(200\mu\text{m})^2$ around the center of the target in the $x - z$ plane. PPS stands for pepper-pot screen.

Target/ Run label	slanted slots	layer thickness	layer material	wall thickness	wall material	T_e (eV) at 10ns	B (kGauss) at 10ns
A	Yes	$15\mu\text{m}$	Mg	$100\mu\text{m}$	Be	25	158
B	No	$6\mu\text{m}$	Cu	$150\mu\text{m}$	CH	26	152
C	No	$6\mu\text{m}$	CH	$150\mu\text{m}$	CH	28	86

(2) opened window on the wall for reducing the diffusion of proton beams.

A. Hydrodynamics

We show the evolution of density, electron temperature and X-ray flux in the first three rows in Fig. 2 to 4. The gold plugs hold back the shock at one end of each half-cylinder of foam. Two shocks of roughly same strength in the same material propagate from opposite directions towards the center of the tube. The layer placed in the middle between the two regions collimates the shocked flows and introduces a length scale through its thickness which will influence the dominant modes of the resulting shear instability. The cut slots in the layer introduce alternating density gradients and causes magnetic field generation by Biermann battery term, which is discussed in Sec. III C. Because the layer does not fully collimate the shocks, oblique shocks are launched into the opposite volumes of the tube. The shock front near the end of the tube travels further transversely. It takes roughly 8.5ns for the shocks to cross and create the pressure-balanced shear mixing region. The pressure in the two regions is roughly equal and the shocked material is the same on each side of the mixing layer, so that the mixing region does not experience a net translation away from the center of the shock tube. After 8.5ns, the oblique shock on either end of the tube gradually crosses the primary shock from the other direction. An oblique region of high density is developed by the reverse shock.

The ideally constructed target should be symmetric about a rotation of 180 degrees. However, the different effective laser intensities on two ends of the target due to different laser incident angles cause the two shocks to move at slightly different speeds. The shock from the right side in Fig. 2 to 4, moves slightly faster. This asymmetry does not affect the overall picture of the hydrodynamical and magnetic field evolution, but the asymmetry of the density distribution can affect the proton radiography which is discussed in Sec. III D.

Because of the opened window on the wall, there are plasma plumes traveling outside the window. As shown in Fig. 5, the overall picture of hydrodynamical evolution is still similar to previous shock-shear experiments without a window[28, 30, 34, 35], although the plasma plume carries mass and energy away from the tube. At

later times, the shock can penetrate through the wall. This results in plumes outside the wall, which can then interact with the plume from the window.

B. X-ray images

The transmitted X-ray flux is shown in the third rows in Fig. 2 to 4. In the X-ray flux, the location and the shape of the shock front is consistent with the density distribution and can be easily identified. The shocks in the wall can also be seen in the X-ray image. The plume launched from the wall or the window has low density and is not visible in the X-ray flux. The layer has high density and low X-ray transmission, leading to the low flux on the X-ray image. For runA and runB, where the layer material is magnesium and copper respectively, the contrast of X-ray flux between the layer and the foam is high, while for runC where the layer material is CH, the X-ray contrast is low.

C. Magnetic fields

When the shock from one end of the tube passes, the temperature is high near the center of the half-cylinder as shown in the second rows in Fig. 2 to 4. A cold region is left behind the shock. The temperature gradient near the layer is perpendicular to the layer and pointing towards the shocked region, due to electron heat conduction. The density gradient is alternating, caused by the cut slots on the layer. Thus the Biermann battery term generates the alternating magnetic field in the $\pm y$ direction, as shown in Fig. 6(a). However, the cold region left behind the shock has low electron temperature and thus high resistivity. The magnetic fields behind the shock diffuse very quickly. In the end, the only significant field left near the center of the tube is in the $-y$ direction, because near the center of the tube, the layer is at high density instead of at a cut slot. On both sides of that high density layer, the field generation is in the $-y$ direction. Two shocks from two ends of the tube cross, amplify the magnetic field and create a doubly shocked, high temperature region, which has low resistivity and the field is less diffusive.

The magnetic field in the plume traveling outside the window is generated in a similar way to the magnetic field generated in the ablation plume of a laser inter-

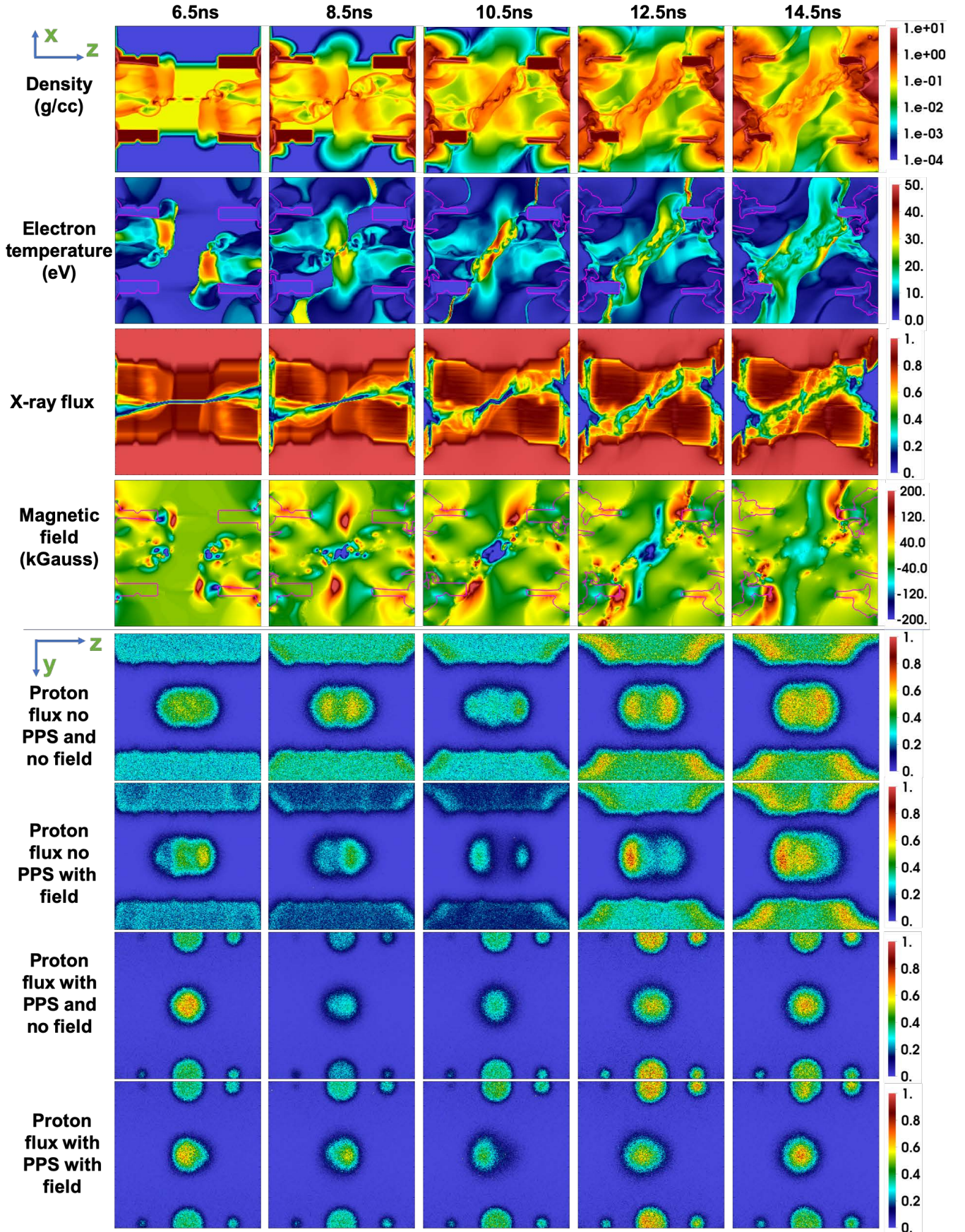


Figure 2: Spatial distribution of different quantities at different time. The size of all plots is $1200\mu\text{m} \times 1200\mu\text{m}$.

From first to fourth row are: density at the $y = 0$ plane, electron temperature at the $y = 0$ plane, X-ray flux normalized by the purely transparent flux, magnetic field B_y in kGauss at $y = 0$ plane (positive for into the plane). The plots in the second and the fourth rows are overlaid with magenta contours for the density of the wall material equal to 0.5g/cc. From fifth to the last rows are proton images for four different cases as labeled.

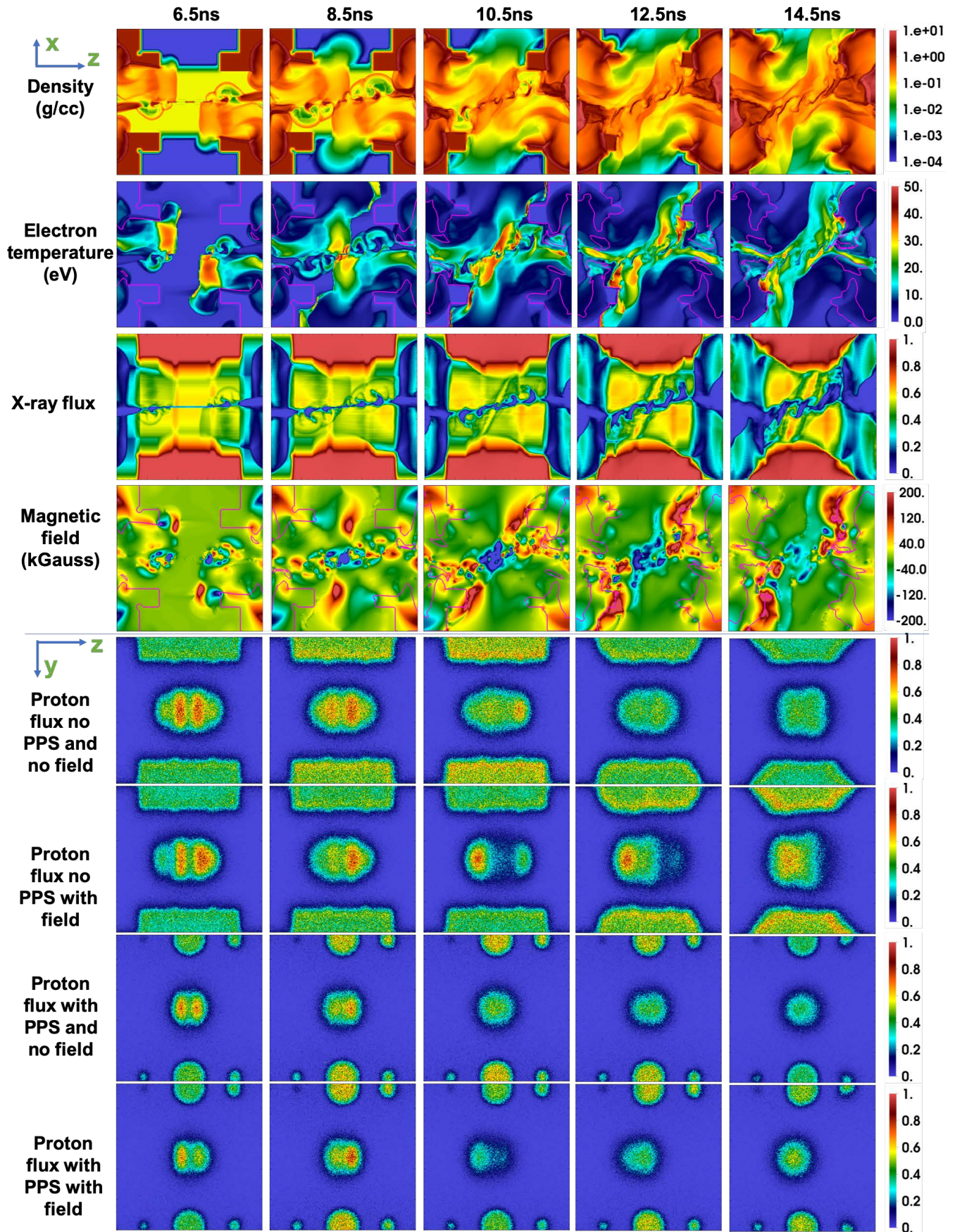


Figure 3: Same as Fig. 2 but for runB

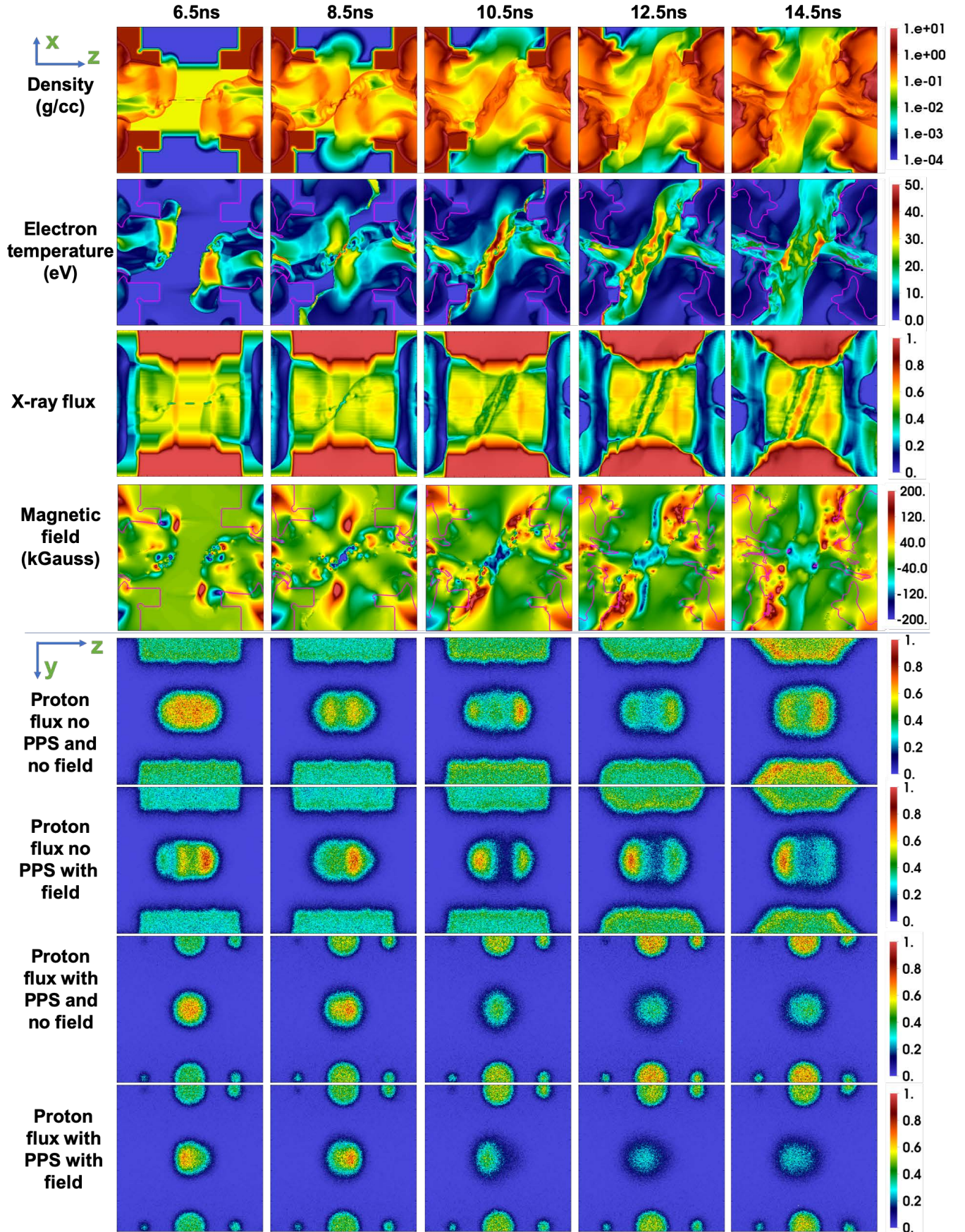


Figure 4: Same as Fig. 2 but for runC

Table II: Simulated plasma properties for runA. All quantities are in cgs units except temperature, which is expressed in eV. The length scale, L is approximately the diameter of the tube ($\approx 500\mu\text{m}$). The n_e , ρ , T_e and T_i are calculated by averaging over a $(200^2\mu\text{m})^2$ square around the center of the target in the $x-z$ plane, at $t = 10\text{ns}$. The flow speed is $u = 7 \times 10^6\text{cm/s}$ for each counter propagating flow.

Plasma property	Formula	Value at $r = 0$
Electron density $n_e(\text{cm}^{-3})$...	5.6×10^{22}
Mass density $\rho(\text{g/cm}^3)$...	0.36
Electron temperature $T_e(\text{eV})$...	25
Ion temperature $T_i(\text{eV})$...	25
Magnetic field B (gauss)	...	1.6×10^5
Average ionization Z	...	1.9
Average atomic weight A	...	7.3
Flow speed $u(\text{cm/s})$...	7×10^6
Sound speed $c_s(\text{cm/s})$	$\frac{9.8 \times 10^5 [ZT_e + 1.67T_i]^{1/2}}{A^{1/2}}$	3.4×10^6
Mach number M	u/c_s	2
Coulomb logarithm $\ln \Lambda$	$\min(23.5 + \ln(T_e^{1.5}/n_e^{0.5}/Z), 25.3 + \ln(T_e/n_e^{0.5}))$	1.4
Hall parameter χ	$6.1 \times 10^{12} \frac{T_e^{3/2} B}{Z n_e \ln \Lambda}$	8×10^{-4}
Plasma β	$\frac{2.4 \times 10^{-12} n_e (T_e + T_i/Z)}{B^2/(8\pi)}$	5×10^3
Péclet number Pe	$uL/(\frac{\kappa_e}{\frac{3}{2}n_e k_B})(\frac{\kappa_e}{\frac{3}{2}n_e k_B} = 5.5 \times 10^{21} \frac{T_e^{5/2}}{n_e(3.3+Z)\ln \Lambda})$	8.3×10^3
Magnetic Reynolds number Rm	$uL/\eta \left(\eta = 8.2 \times 10^5 \frac{(0.33Z+0.18)\ln \Lambda}{T_e^{3/2}} \right)$	47
Reynolds number Re	$uL/\nu \left(\nu = 1.9 \times 10^{19} \frac{T_i^{5/2}}{A^{1/2} Z^3 n_e \ln \Lambda} \right)$	8.6×10^6

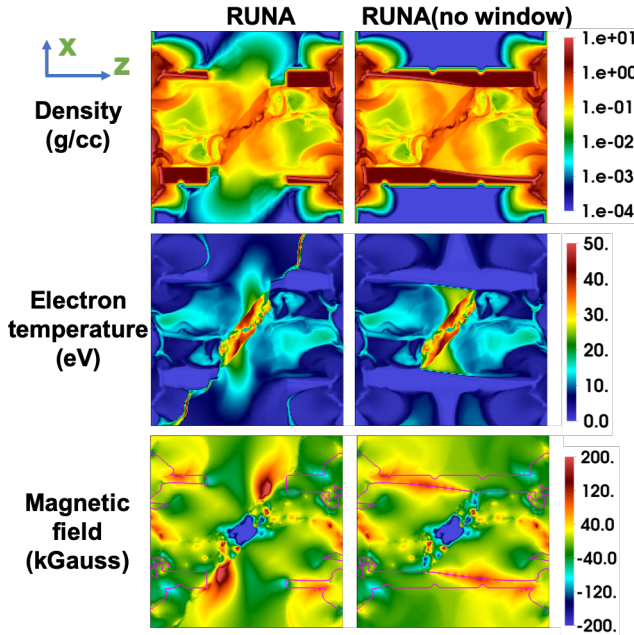


Figure 5: Spatial distribution of different quantities for runA with or without window at 10ns. The size of all plots is $1200\mu\text{m} \times 1200\mu\text{m}$. From first to last row are: density at the $y = 0$ plane, electron temperature at the $y = 0$ plane, magnetic field B_y in kGauss at $y = 0$ plane (positive for into the plane). The plots in the second row are overlaid with magenta contours for the density of the wall material equal to 0.5g/cc .

action with a solid target[9, 10, 12, 13]. The plume is continuously launched by the flow inside the shock tube and expands in all directions, with the density gradient to point towards the dense part of the plume, as shown in Fig. 6(b). The temperature gradient along the outflow direction is reduced due to electron thermal conduction, but the temperature gradient perpendicular to the outflow direction survives due to continuous launching of the plume from the shock tube. Thus the magnetic field generated by the Biermann battery term is into the plane on the right side and out of the plane on the left side in Fig. 6(b).

The magnetic field evolution is shown in the fourth row in Fig. 2 to 4. In the center of the tube, a field pointing in $-y$ direction dominates. Outside the window, the field pointing in $+y$ direction survives, while the field pointing in $-y$ direction diffuses quickly due to low temperature and high resistivity. The total magnetic flux in the $y = 0$ plane is conserved and vanishes. We are interested in the magnetic field near the center of the tube which can potentially affect the mix. The magnetic field outside the window plays a role in the proton radiography as discussed in Sec. IIID, but we are not interested in its dynamical importance because it is far away from the mix region. As shown in Fig. 5, the magnetic field near the center of the tube is similar between the runs with and without the window.

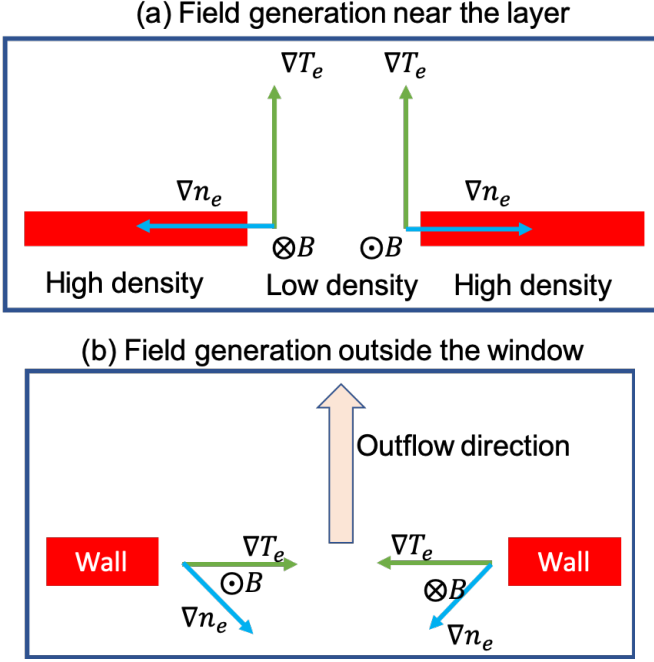


Figure 6: Schematics of the magnetic field generation by Biermann battery term ($\nabla n_e \times \nabla T_e$). (a) Near the layer, the temperature gradient is perpendicular to the layer due to thermal conduction, the density gradient is alternating and along the layer due to the cut slots on the layer, so that the Biermann generated field is alternating into and out of the plane. (b) Outside the window, the density gradient points to the dense part of the plume, the temperature gradient along the outflow direction is small due to conduction, but the temperature gradient perpendicular to the outflow direction survives due to continuous launching of the plume from the shock tube, thus the field is into the plane on the right side and out of the plane on the left side.

D. Proton radiography

We use the MPRAD code[25] to simulate the proton image by taking the output data from 3D FLASH simulations. In the simulations, we use a typical size $45\mu\text{m}$ for proton source. We find that the features of the proton images are most prominent in 14.3MeV to 14.5MeV band, i.e. protons losing between 0.2MeV and 0.4MeV of kinetic energy. We compare the proton images with/without field, and with/without pepper pot screen (PPS) in the fifth to the last rows in Fig. 2 to 4. To quantify the asymmetry of the proton image, the averaged horizontal proton position in the blob at the center of the proton image is plotted in Fig. 7. The ideally constructed target should be symmetric about a rotation of 180 degrees and the proton image should also be symmetric in the absence of magnetic field. The asymmetry of the proton image about the vertical axis can be interpreted

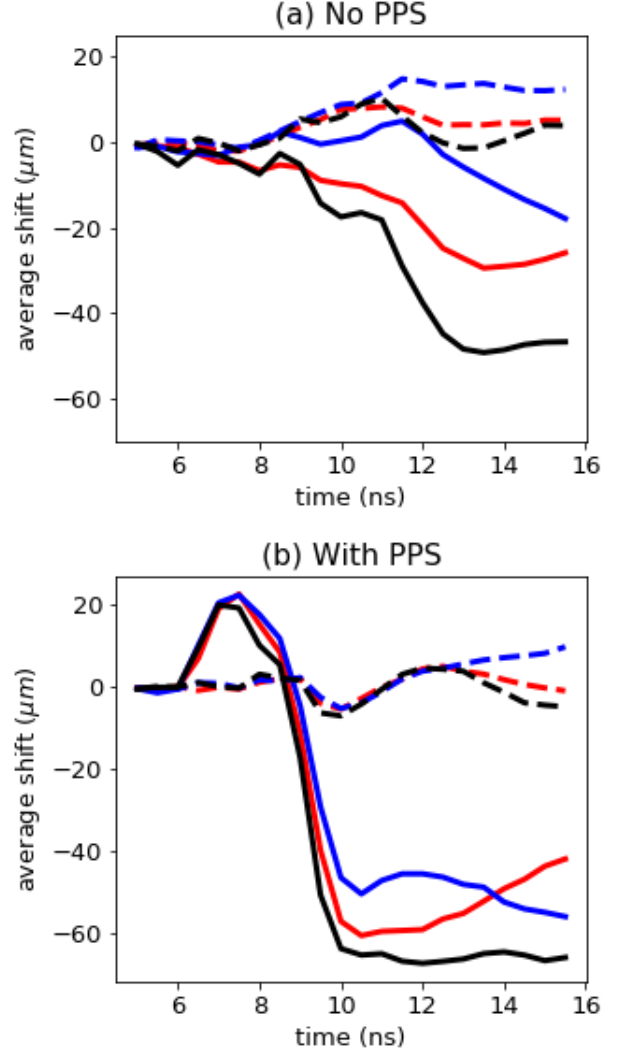


Figure 7: The evolution of the averaged position of protons in the blob in final energy range 14.3MeV to 14.5MeV. The scale is divided by the magnification to align with the scales on the target system. The red curves are for runA, the black curves are for runB, and the blue curves are for runC. The dashed curves are for the MPRAD runs with magnetic field turned off, and the solid curves are for MPRAD runs with magnetic field turned on. (a) is for no PPS case and (b) is for with PPS case.

as the existence of magnetic field.

However, in the no PPS case, i.e. the fifth rows in Fig. 2 to 4, the blob in the middle of the image can be slightly asymmetric even without magnetic field. This asymmetry is not as large as the asymmetry in the images where there is field but no PPS, i.e. the six rows, which means the proton deflection by magnetic field causes more asymmetry than by the density asymmetry due to the fact that the shock from the right side in Fig. 2 to 4, moves slightly faster. This slight difference is caused by the different ef-

fective laser intensities on two ends of the target due to different laser incident angles. In the simulations in this work, we do not take into account the unevenness of the foam and the power imbalance on two ends of the tube, which can potentially cause more the asymmetry on the proton image than what we show in this work.

One advantage of using PPS is that the viewing of the surrounding holes is through the regions without the field and the viewing of the hole in the middle is only thorough the region with magnetic field, so that the net deflection caused by the magnetic field can be determined without another control shot using same target. With PPS, the asymmetry in the no field case, i.e. the seventh row in Fig. 2 to 4, is significantly less than the without field and without PPS case, i.e. the fifth rows. The PPS is very efficient in reducing the asymmetry of the proton image cause by the intensity imbalance on two ends and the unevenness of the foam. As shown in Fig. 7(b), the asymmetry caused by the proton deflection is significantly larger than that caused by the ununiform density. The blob has a positive net shift at early time, because of the field pointing in $+y$ direction in the plume outside the window. At about 8.5ns, the proton deflection caused by the field pointing in $+y$ direction in the plume outside the window and by the field in near the center of the tube pointing in $-y$ direction cancels, resulting in zero net shift of the blob on the proton image. At a late time $t > 10$ ns, the field pointing in $+y$ direction moves away from the $z = 0$ plane, but the field near the center of the tube has no net advection, and the net shift of the blob is negative. The shift value on the image plate divided by the magnification can reach 50 to 70 μ m. The difference between the early time shift and late time shift can reach 70 to 90 μ m. The prediction for the net shift of the blob will be compared to the experimental data to validate the magnetic field model in FLASH.

IV. CONCLUSIONS AND DISCUSSIONS

We carried out the radiation-MHD simulations and predicted the X-ray and proton images by synthetic radiographs. The hydrodynamical evolution can be measured using XRFC and compared with the simulation results. The predicted proton radiography shows the direction and the amount of the shift of the proton beam going through the window and/or PPS. Although the target can diffuse the proton beam significantly, the evolution of the shift in the synthetic proton radiography is still consistent with the evolution of the magnetic fields in the target system and shows change between early time and late time. However, the prediction only shows the signal contribution from the mean magnetic fields from different columns along the line of sight. The signal from small scale fields always gets damped by the diffusion of the proton beam. High energy proton beam accelerated by Target Normal Sheath Acceleration (TNSA) mechanism using OMEGA EP beam experiences less diffusion

through the target[70]. The Coulomb scattering angle is roughly proportional to E_p^{-2} where E_p is the kinetic energy of the proton[25, 63, 64].

The simulation shows that the design we use can achieve a regime with high plasma beta β . The Hall parameter χ , defined by the ratio of electron gyro-frequency to electron collision frequency, is small. The Reynold number Re is high enough to ensure turbulence, and the magnetic Reynolds number Rm is around 50. Under the condition with these dimensionless parameters, the magnetic field remains dynamically unimportant. The magnetic energy density from Table II is 10⁹erg/s, which is only 0.3% of the turbulent kinetic energy reported in the simulation in Ref. [35] for a previous mix modeling for shock-shear targets under similar condition to this work. Thus the magnetic field is also negligible for mix modeling in the shock-shear targets. It is desirable to optimize the measurable magnetic fields and improve the dynamical importance of the magnetic fields.

The Biermann battery generated magnetic field is roughly $\frac{ck_B T_e}{eLu}$ by balancing the Biermann battery term with the advection term. The plasma beta β is then proportional to $\frac{n_e T_e}{(T_e/Lu)^2} \propto \frac{n_e u^2}{L^2 T_e}$. If we keep the size of the target and the laser power, then $n_e u^2$ and L are roughly constants, then $\beta \propto \frac{1}{T_e}$. Thus increasing T_e can reduce β and make the Lorentz force more important. The Hall parameter[52] χ is proportional to $\frac{T_e^{3/2}}{n_e}$ and the magnetic Reynolds number Rm is proportional to $T_e^{3/2}$. Both χ and Rm increase with temperature. For low Rm and low magnetic Prandtl number Pr_m , i.e. $Pr_m = Rm/Re \ll 1$, the power spectrum of the kinetic energy $E(k)$ and the power spectrum of the magnetic energy $M(k)$ are related by $M(k) \propto k^{-2}E(k)$, and $M(k)$ is always softer than $E(k)$, and the magnetic field remains dynamically unimportant even in small scales[20, 71, 72]. High Rm is favorable for the amplification of magnetic fields and a hard power law for magnetic energy spectrum[21, 71, 73]. One way to achieve a higher temperature is to lower the density of the foam. However, making a low density foam in the target is challenging for target fabrication. It causes the unevenness in the foam, leads to the unevenness of the proton image, and makes it difficult to interpret the experimental data from proton radiography. In a low density foam, the flow may move too fast so that the time window for diagnostics is narrow.

Some experiments[74] and theories[75, 76] show that around 10eV the value of electrical resistivity (electrical resistivity η is related to magnetic resistivity η_B by $\eta_B = \frac{c^2}{4\pi}\eta$) is different from the Spitzer resistivity. However, the electrical resistivity with temperature and density dependency under the condition of our experiment design is not well constrained. If the modeling in this work is correct in terms of electrical resistivity, then this would indicate that the magnetic field may not be dynamically important. However, if the electrical resistivity is significantly lower than the Spitzer resistivity that we use in this work, then the code underestimates the mag-

netic fields, and the mix model could potentially cover up the magnetic field effects by the choice of the initial input conditions for the model. Future experiments executed at higher temperatures can potentially make magnetic fields start to play a more important role. In the future development of the simulations, the implementation of implicit method for the magnetic diffusion equation is desirable for the case of large resistivity where fully explicit method requires small time step.

V. ACKNOWLEDGEMENTS

Research presented in this paper was supported by the Laboratory Directed Research and Develop-

ment(LDRD) program 20180040DR of Los Alamos National Laboratory(LANL). The simulations were performed with LANL Institutional Computing which is supported by the U.S. Department of Energy National Nuclear Security Administration under Contract No. 89233218CNA000001, and with the Extreme Science and Engineering Discovery Environment (XSEDE), which is supported by National Science Foundation(NSF) grant number ACI-1548562.

-
- [1] C. R. Weber, D. S. Clark, A. W. Cook, L. E. Busby, and H. F. Robey, *Phys. Rev. E* **89**, 053106 (2014).
 - [2] D. S. Clark, M. M. Marinak, C. R. Weber, D. C. Eder, S. W. Haan, B. A. Hammel, D. E. Hinkel, O. S. Jones, J. L. Milovich, P. K. Patel, H. F. Robey, J. D. Salmonson, S. M. Sepke, and C. A. Thomas, *Physics of Plasmas* **22**, 022703 (2015).
 - [3] B. M. Haines, E. L. Vold, K. Molvig, C. Aldrich, and R. Rauenzahn, *Physics of Plasmas* **21**, 092306 (2014).
 - [4] B. M. Haines, G. P. Grim, J. R. Fincke, R. C. Shah, C. J. Forrest, K. Silverstein, F. J. Marshall, M. Boswell, M. M. Fowler, R. A. Gore, A. C. Hayes-Sterbenz, G. Jungman, A. Klein, R. S. Rundberg, M. J. Steinkamp, and J. B. Wilhelmy, *Physics of Plasmas* **23**, 072709 (2016).
 - [5] T. Haxhimali, R. E. Rudd, W. H. Cabot, and F. R. Graziani, *Physical Review E* **92** (2015), 10.1103/physreve.92.053110.
 - [6] E. L. Vold, A. S. Joglekar, M. I. Ortega, R. Moll, D. Fenn, and K. Molvig, *Physics of Plasmas* **22**, 112708 (2015).
 - [7] E. Vold, A. Joglekar, M. Ortega, R. Moll, D. Fenn, and K. Molvig, *Journal of Physics: Conference Series* **717**, 012056 (2016).
 - [8] L. Biermann, *Zeitschrift Naturforschung Teil A* **5**, 65 (1950).
 - [9] C. K. Li, F. H. Séguin, J. A. Frenje, J. R. Rygg, R. D. Petrasso, R. P. J. Town, P. A. Amendt, S. P. Hatchett, O. L. Landen, A. J. Mackinnon, P. K. Patel, V. A. Smalyuk, T. C. Sangster, and J. P. Knauer, *Physical Review Letters* **97** (2006), 10.1103/physrevlett.97.135003.
 - [10] C. A. Cecchetti, M. Borghesi, J. Fuchs, G. Schurtz, S. Kar, A. Macchi, L. Romagnani, P. A. Wilson, P. Antici, R. Jung, J. Osterholtz, C. A. Pipahl, O. Willi, A. Schiavi, M. Notley, and D. Neely, *Physics of Plasmas* **16**, 043102 (2009).
 - [11] L. Gao, E. Liang, Y. Lu, R. K. Follet, H. Sio, P. Tzeferacos, D. H. Froula, A. Birkel, C. K. Li, D. Lamb, R. Petrasso, W. Fu, M. Wei, and H. Ji, *The Astrophysical Journal* **873**, L11 (2019).
 - [12] C. K. Li, F. H. Séguin, J. A. Frenje, J. R. Rygg, R. D. Petrasso, R. P. J. Town, P. A. Amendt, S. P. Hatchett, O. L. Landen, A. J. Mackinnon, P. K. Patel, M. Tabak, J. P. Knauer, T. C. Sangster, and V. A. Smalyuk, *Physical Review Letters* **99** (2007), 10.1103/physrevlett.99.015001.
 - [13] C. K. Li, F. H. Séguin, J. A. Frenje, M. Manuel, D. Casey, N. Sinenian, R. D. Petrasso, P. A. Amendt, O. L. Landen, J. R. Rygg, R. P. J. Town, R. Betti, J. Delettrez, J. P. Knauer, F. Marshall, D. D. Meyerhofer, T. C. Sangster, D. Shvarts, V. A. Smalyuk, J. M. Soures, C. A. Back, J. D. Kilkenny, and A. Nikroo, *Physics of Plasmas* **16**, 056304 (2009).
 - [14] C. K. Li, D. D. Ryutov, S. X. Hu, M. J. Rosenberg, A. B. Zylstra, F. H. Séguin, J. A. Frenje, D. T. Casey, M. G. Johnson, M. J.-E. Manuel, H. G. Rinderknecht, R. D. Petrasso, P. A. Amendt, H. S. Park, B. A. Remington, S. C. Wilks, R. Betti, D. H. Froula, J. P. Knauer, D. D. Meyerhofer, R. P. Drake, C. C. Kuranz, R. Young, and M. Koenig, *Physical Review Letters* **111** (2013), 10.1103/physrevlett.111.235003.
 - [15] R. D. Petrasso, C. K. Li, F. H. Seguin, J. R. Rygg, J. A. Frenje, R. Betti, J. P. Knauer, D. D. Meyerhofer, P. A. Amendt, D. H. Froula, O. L. Landen, P. K. Patel, J. S. Ross, and R. P. J. Town, *Physical Review Letters* **103** (2009), 10.1103/physrevlett.103.085001.
 - [16] G. Gregori, A. Ravasio, C. D. Murphy, K. Schaar, A. Baird, A. R. Bell, A. Benuzzi-Mounaix, R. Bingham, C. Constantin, R. P. Drake, M. Edwards, E. T. Everson, C. D. Gregory, Y. Kuramitsu, W. Lau, J. Mithen, C. Niemann, H.-S. Park, B. A. Remington, B. Reville, A. P. L. Robinson, D. D. Ryutov, Y. Sakawa, S. Yang, N. C. Woolsey, M. Koenig, and F. Miniati, *Nature* **481**, 480 (2012).
 - [17] A. Nishiguchi, T. Yabe, M. G. Haines, M. Psimopoulos, and H. Takewaki, *Physical Review Letters* **53**, 262 (1984).
 - [18] C. Walsh, J. Chittenden, K. McGlinchey, N. Niasse, and B. Appelbe, *Physical Review Letters* **118** (2017), 10.1103/physrevlett.118.155001.
 - [19] C. A. Walsh, K. McGlinchey, J. K. Tong, B. D. Appelbe, A. Crilly, M. F. Zhang, and J. P. Chittenden, *Physics of Plasmas* **26**, 022701 (2019).
 - [20] J. Meinecke, H. W. Doyle, F. Miniati, A. R. Bell, R. Bingham, R. Crowston, R. P. Drake, M. Fatenejad, M. Koenig, Y. Kuramitsu, C. C. Kuranz, D. Q. Lamb, D. Lee, M. J. MacDonald, C. D. Murphy, H.-S. Park, A. Pelka, A. Ravasio, Y. Sakawa, A. A. Schekochihin,

- A. Scopatz, P. Tzeferacos, W. C. Wan, N. C. Woolsey, R. Yurchak, B. Reville, and G. Gregori, *Nature Physics* **10**, 520 (2014).
- [21] P. Tzeferacos, A. Rigby, A. F. A. Bott, A. R. Bell, R. Bingham, A. Casner, F. Cattaneo, E. M. Churazov, J. Emig, F. Fiuza, C. B. Forest, J. Foster, C. Graziani, J. Katz, M. Koenig, C.-K. Li, J. Meinecke, R. Petrasso, H.-S. Park, B. A. Remington, J. S. Ross, D. Ryu, D. Ryutov, T. G. White, B. Reville, F. Miniati, A. A. Schekochihin, D. Q. Lamb, D. H. Froula, and G. Gregori, *Nature Communications* **9** (2018), 10.1038/s41467-018-02953-2.
- [22] T. G. White, M. T. Oliver, P. Mabey, M. KÄEhn-Kauffeldt, A. F. A. Bott, L. N. K. DÄ¶hl, A. R. Bell, R. Bingham, R. Clarke, J. Foster, G. Giacinti, P. Graham, R. Heathcote, M. Koenig, Y. Kuramitsu, D. Q. Lamb, J. Meinecke, T. Michel, F. Miniati, M. Notley, B. Reville, D. Ryu, S. Sarkar, Y. Sakawa, M. P. Selwood, J. Squire, R. H. H. Scott, P. Tzeferacos, N. Woolsey, A. A. Schekochihin, and G. Gregori, *Nature Communications* **10** (2019), 10.1038/s41467-019-09498-y.
- [23] L. Welser-Sherrill, J. Fincke, F. Doss, E. Loomis, K. Flippo, D. Offermann, P. Keiter, B. Haines, and F. Grinstein, *High Energy Density Physics* **9**, 496 (2013).
- [24] D. Capelli, D. W. Schmidt, T. Cardenas, G. Rivera, R. B. Randolph, F. Fierro, E. C. Merritt, K. A. Flippo, F. W. Doss, and J. L. Kline, *Fusion Science and Technology* **70**, 316 (2016).
- [25] Y. Lu, H. Li, K. A. Flippo, K. Kelso, A. Liao, S. Li, and E. Liang, Submitted to Review of Scientific Instruments (2019).
- [26] K. A. Flippo, F. W. Doss, B. DeVolder, J. R. Fincke, E. N. Loomis, J. L. Kline, and L. Welser-Sherrill, *Journal of Physics: Conference Series* **688**, 012018 (2016).
- [27] K. Flippo, F. Doss, J. Kline, E. Merritt, D. Capelli, T. Cardenas, B. DeVolder, F. Fierro, C. Huntington, L. Kot, E. Loomis, S. MacLaren, T. Murphy, S. Nagel, T. Perry, R. Randolph, G. Rivera, and D. Schmidt, *Physical Review Letters* **117** (2016), 10.1103/physrevlett.117.225001.
- [28] E. Merritt, F. Doss, C. D. Stefano, K. Flippo, A. Rasmus, and D. Schmidt, *High Energy Density Physics* **23**, 90 (2017).
- [29] F. W. Doss, J. L. Kline, K. A. Flippo, T. S. Perry, B. G. DeVolder, I. Tregillis, E. N. Loomis, E. C. Merritt, T. J. Murphy, L. Welser-Sherrill, and J. R. Fincke, *Physics of Plasmas* **22**, 056303 (2015).
- [30] E. C. Merritt, F. W. Doss, E. N. Loomis, K. A. Flippo, and J. L. Kline, *Physics of Plasmas* **22**, 062306 (2015).
- [31] K. A. Flippo, F. W. Doss, E. C. Merritt, B. G. DeVolder, C. A. D. Stefano, P. A. Bradley, D. Capelli, T. Cardenas, T. R. Desjardins, F. Fierro, C. M. Huntington, J. L. Kline, L. Kot, S. Kurien, E. N. Loomis, S. A. MacLaren, T. J. Murphy, S. R. Nagel, T. S. Perry, R. B. Randolph, A. Rasmus, and D. W. Schmidt, *Physics of Plasmas* **25**, 056315 (2018).
- [32] F. W. Doss, K. A. Flippo, D. Capelli, T. Cardenas, B. DeVolder, J. Kline, L. Kot, S. Kurien, E. Loomis, E. C. Merritt, T. Perry, D. Schmidt, and C. D. Stefano, *Journal of Physics: Conference Series* **717**, 012059 (2016).
- [33] F. W. Doss, K. A. Flippo, and E. C. Merritt, *Physical Review E* **94** (2016), 10.1103/physreve.94.023101.
- [34] F. W. Doss, J. R. Fincke, E. N. Loomis, L. Welser-Sherrill, and K. A. Flippo, *Physics of Plasmas* **20**, 122704 (2013).
- [35] F. W. Doss, E. N. Loomis, L. Welser-Sherrill, J. R. Fincke, K. A. Flippo, and P. A. Keiter, *Physics of Plasmas* **20**, 012707 (2013).
- [36] P. Wang, Y. Zhou, S. A. MacLaren, C. M. Huntington, K. S. Raman, F. W. Doss, and K. A. Flippo, *Physics of Plasmas* **22**, 112701 (2015).
- [37] A. Banerjee, R. A. Gore, and M. J. Andrews, *Physical Review E* **82** (2010), 10.1103/physreve.82.046309.
- [38] B. M. Haines, F. F. Grinstein, and J. D. Schwarzkopf, *Journal of Turbulence* **14**, 46 (2013).
- [39] B. Fryxell, K. Olson, P. Ricker, F. X. Timmes, M. Zingale, D. Q. Lamb, P. MacNeice, R. Rosner, J. W. Truran, and H. Tufo, *The Astrophysical Journal Supplement Series* **131**, 273 (2000).
- [40] A. Dubey, K. Antypas, M. K. Ganapathy, L. B. Reid, K. Riley, D. Sheeler, A. Siegel, and K. Weide, *Parallel Computing* **35**, 512 (2009).
- [41] T. Boehly, D. Brown, R. Craxton, R. Keck, J. Knauer, J. Kelly, T. Kessler, S. Kumpan, S. Loucks, S. Letzring, F. Marshall, R. McCrory, S. Morse, W. Seka, J. Soures, and C. Verdon, *Optics Communications* **133**, 495 (1997).
- [42] L. R. Benedetti, P. M. Bell, D. K. Bradley, C. G. Brown, S. M. Glenn, R. Heeter, J. P. Holder, N. Izumi, S. F. Khan, G. Lacaille, N. Simanovskaia, V. A. Smalyuk, and R. Thomas, *Review of Scientific Instruments* **83**, 10E135 (2012).
- [43] D. K. Bradley, P. M. Bell, J. D. Kilkenny, R. Hanks, O. Landen, P. A. Jaanimagi, P. W. McKenty, and C. P. Verdon, *Review of Scientific Instruments* **63**, 4813 (1992).
- [44] D. K. Bradley, P. M. Bell, O. L. Landen, J. D. Kilkenny, and J. Oertel, *Review of Scientific Instruments* **66**, 716 (1995).
- [45] FLASH4 is available at <https://flash.uchicago.edu/>.
- [46] P. Roe, *Journal of Computational Physics* **43**, 357 (1981).
- [47] S. Li, *Journal of Computational Physics* **203**, 344 (2005).
- [48] T. Miyoshi and K. Kusano, *Journal of Computational Physics* **208**, 315 (2005).
- [49] E. F. Toro, *Riemann Solvers and Numerical Methods for Fluid Dynamics* (Springer Berlin Heidelberg, 2009).
- [50] R. D. Falgout and U. M. Yang, in *Lecture Notes in Computer Science* (Springer Berlin Heidelberg, 2002) pp. 632–641.
- [51] L. Spitzer and R. J. Seeger, *American Journal of Physics* **31**, 890 (1963).
- [52] S. I. Braginskii, *Reviews of Plasma Physics* **1**, 205 (1965).
- [53] D. S. Balsara and D. S. Spicer, *Journal of Computational Physics* **149**, 270 (1999).
- [54] C. Graziani, P. Tzeferacos, D. Lee, D. Q. Lamb, K. Weide, M. Fatenejad, and J. Miller, *The Astrophysical Journal* **802**, 43 (2015).
- [55] M. Gittings, R. Weaver, M. Clover, T. Betlach, N. Byrne, R. Coker, E. Dendy, R. Hueckstaedt, K. New, W. R. Oakes, D. Ranta, and R. Stefan, *Computational Science & Discovery* **1**, 015005 (2008).
- [56] B. M. Haines, C. H. Aldrich, J. M. Campbell, R. M. Rauenzahn, and C. A. Wingate, *Physics of Plasmas* **24**, 052701 (2017).
- [57] J. MacFarlane, I. Golovkin, and P. Woodruff, *Journal of Quantitative Spectroscopy and Radiative Transfer* **99**, 381 (2006).
- [58] Prism Computational Sciences
PrOpacEOS Overview <http://www.prism-cs.com/Software/Propaceos/overview.html>.

- [59] E. Brunetti, R. P. Shanks, G. G. Manahan, M. R. Islam, B. Ersfeld, M. P. Anania, S. Cipiccia, R. C. Issac, G. Raj, G. Vieux, G. H. Welsh, S. M. Wiggins, and D. A. Jaroszynski, *Physical Review Letters* **105** (2010), 10.1103/physrevlett.105.215007.
- [60] A. C. Thompson, D. T. Attwood, E. M. Gullikson, M. R. Howells, J. B. Kortright, A. L. Robinson, and J. H. Underwood, *X-ray data booklet*, Vol. 8 (Lawrence Berkeley National Laboratory, University of California Berkeley, CA, 2001).
- [61] J. MacFarlane, I. Golovkin, P. Wang, P. Woodruff, and N. Pereyra, *High Energy Density Physics* **3**, 181 (2007).
- [62] Prism Computational Sciences SPECT3D Overview <http://www.prism-cs.com/Software/Spect3D/overview.html>.
- [63] G. Moliere, *Zeitschrift f r Naturforschung A* **3**, 78 (1948).
- [64] H. A. Bethe, *Physical Review* **89**, 1256 (1953).
- [65] H. Bethe, *Annalen der Physik* **397**, 325 (1930).
- [66] E. Bonderup and P. Hvelplund, *Physical Review A* **4**, 562 (1971).
- [67] C.-K. Li and R. D. Petrasso, *Physical Review Letters* **70**, 3059 (1993).
- [68] D. GERICKE, *Laser and Particle Beams* **20**, 471 (2002).
- [69] A. Zylstra, J. Frenje, P. Grabowski, C. Li, G. Collins, P. Fitzsimmons, S. Glenzer, F. Graziani, S. Hansen, S. Hu, M. G. Johnson, P. Keiter, H. Reynolds, J. Rygg, F. S guin, and R. Petrasso, *Physical Review Letters* **114** (2015), 10.1103/physrevlett.114.215002.
- [70] A. B. Zylstra, C. K. Li, H. G. Rinderknecht, F. H. S guin, R. D. Petrasso, C. Stoeckl, D. D. Meyerhofer, P. Nilson, T. C. Sangster, S. L. Pape, A. Mackinnon, and P. Patel, *Review of Scientific Instruments* **83**, 013511 (2012).
- [71] A. A. Schekochihin, A. B. Iskakov, S. C. Cowley, J. C. McWilliams, M. R. E. Proctor, and T. A. Yousef, *New Journal of Physics* **9**, 300 (2007).
- [72] P. Odier, J.-F. Pinton, and S. Fauve, *Physical Review E* **58**, 7397 (1998).
- [73] P. Tzeferacos, A. Rigby, A. Bott, A. R. Bell, R. Bingham, A. Casner, F. Cattaneo, E. M. Churazov, J. Emig, N. Flocke, F. Fiuza, C. B. Forest, J. Foster, C. Graziani, J. Katz, M. Koenig, C.-K. Li, J. Meinecke, R. Petrasso, H.-S. Park, B. A. Remington, J. S. Ross, D. Ryu, D. Ryutov, K. Weide, T. G. White, B. Reville, F. Miniati, A. A. Schekochihin, D. H. Froula, G. Gregori, and D. Q. Lamb, *Physics of Plasmas* **24**, 041404 (2017).
- [74] R. L. Shepherd, D. R. Kania, and L. A. Jones, *Physical Review Letters* **61**, 1278 (1988).
- [75] P. Renaudin, C. Blancard, G. Faussurier, and P. Noiret, *Physical Review Letters* **88** (2002), 10.1103/physrevlett.88.215001.
- [76] A. P. L. Robinson, H. Schmitz, and P. McKenna, *New Journal of Physics* **17**, 083045 (2015).